

RESEARCH ARTICLE

10.1002/2014JB010939

Key Points:

- Four-dimensional dynamically self-consistent mantle modeling with single-sided subduction
- Spontaneous deformation of subduction trenches into their natural arcuate shape
- Two newly discovered features are “back-slab spiral flow” and “slab tunneling”

Correspondence to:

F. Cramer,
fabio.cramer@erdw.ethz.ch

Citation:

Cramer, F., and P. J. Tackley (2014), Spontaneous development of arcuate single-sided subduction in global 3-D mantle convection models with a free surface, *J. Geophys. Res. Solid Earth*, 119, 5921–5942, doi:10.1002/2014JB010939.

Received 3 JAN 2014

Accepted 10 JUN 2014

Accepted article online 16 JUN 2014

Published online 9 JUL 2014

Spontaneous development of arcuate single-sided subduction in global 3-D mantle convection models with a free surface

Fabio Cramer¹ and Paul J. Tackley¹¹Department of Earth Sciences, ETH Zurich, Zurich, Switzerland

Abstract We present temporally evolving 3-D global mantle convection models with single-sided subduction and a free surface in both 3-D Cartesian and fully spherical geometry. Special focus is given to the spontaneous development of three-dimensional structures at the surface and in the upper mantle. We find that an arcuate shape is the natural form for trenches and slabs. Cartesian models are used first to study the dynamic evolution of subduction zones, spreading ridges, and interconnected transform features. These experiments highlight the strong variation of spontaneously developing, arcuate slab curvature and subduction polarity along the trench strike. The spontaneous development of spreading ridges leads to lateral offsets between separated segments that are characterized by normal transform motion. Spherical models then allow insights into the evolution of plate tectonics on a sphere. Investigated are the spontaneous evolution of slab geometry, trench motion, and subduction-induced mantle flow. Two new dynamical features are discovered: “back-slab spiral flow” and “slab tunneling.”

1. Introduction

Subduction zones are one of the most prominent features on a planet that undergoes plate tectonics, not only in terms of surface morphology but also in terms of the planet’s dynamic evolution. Its importance for the dynamics is highlighted by the fact that the sinking portions of a plate (i.e., slabs) are the main drivers of mantle convection and plate tectonics [Forsyth and Uyeda, 1975; Conrad and Lithgow-Bertelloni, 2002]. Dynamical implications of subduction zones are, however, not only limited to plate velocities but find also expression in the strongly time-dependent, strongly three-dimensional flow of slabs, adjacent plates, and mantle.

Another distinctive dynamical feature of a subduction zone is its migration with respect to a “stable” reference frame like the lower mantle. It was noted early on by *Elsasser* [1971] that the Atlantic Ocean is opening in an east-west direction, and the opposite side of the spherical surface (i.e., the Pacific Ocean), therefore, has to shrink accordingly. This implies that the subduction zones in the west and the subduction zones in the east of the Pacific Ocean have to move toward each other, indicating that convergent plate boundaries (subduction trenches) migrate laterally with time. Moreover, it was shown that the constructive (spreading ridges) and conservative plate boundaries (transform faults) also migrate with time [Kaula, 1975].

Trench motions observed on present-day Earth display high variability in direction and magnitude. Trenches migrate not only parallel to but also obliquely to the direction of subducting plate motion. In the first case, trench movement can be advancing (i.e., toward the overriding plate) or retreating (i.e., toward the subducting plate) by performing “slab rollback” [Elsasser, 1971; Garfunkel et al., 1986]. On present-day Earth 75% of trenches retreat and only 25% advance relative to the geodynamically realistic Indo-Atlantic hot spot reference frame [Schellart et al., 2008]. Also, seismological observations indicate a lack of forward draping slab geometries (i.e., roll overs), a distinct characteristic of advancing trenches [e.g., Fukao and Obayashi, 2013]. Three-dimensional models, in contrast, show that slabs can either retreat or advance, depending on the boundary condition at the trailing edge of the subducting plate [e.g., Funicello et al., 2004; Schellart, 2004], the trench-parallel width of the slab [e.g., Schellart, 2004; Morra et al., 2006; Stegman et al., 2006], and the difference between slab and surrounding mantle in strength [e.g., Capitanio et al., 2007; Funicello et al., 2008] and density [e.g., Stegman et al., 2010a]. As on present-day Earth, fully dynamic models prefer trench retreat, except for locations in the center of wide subduction zones [Stegman et al., 2010a, 2010b; Cramer et al., 2012a].

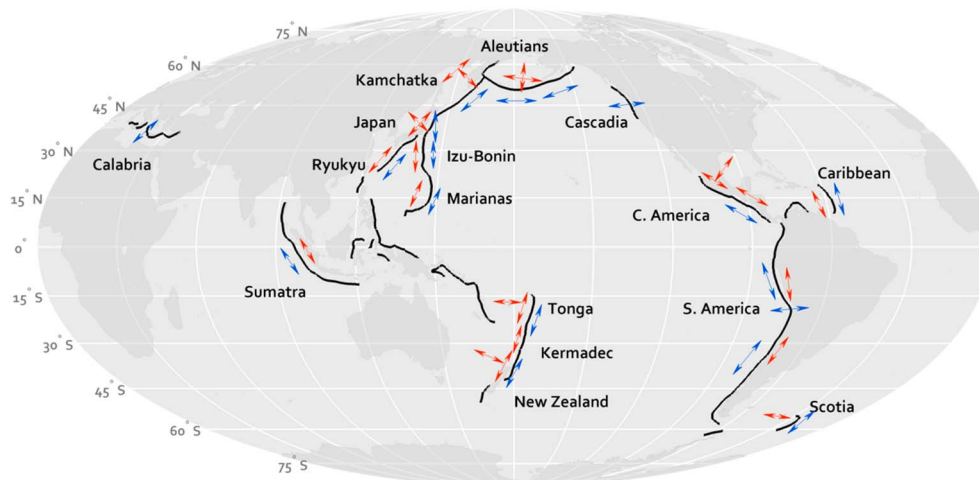


Figure 1. Sketch of constraints on subduction zone anisotropy from shear wave splitting measurements from the compilation presented in Long [2013]. The subduction trenches compiled by Bird [2003] are shown in black. The anisotropic signals of the wedge (red) and back-slab regions (blue) are shown separately. Blue arrows indicate average fast directions for the back-slab splitting signal from SKS (seismic waves traveling through the Outer Core), local S, and source-side teleseismic S-splitting measurements [Long and Silver, 2009; Paczkowski, 2012]. Red arrows indicate average fast directions for wedge anisotropy from local S splitting [Long and Wirth, 2013]. In regions where multiple fast directions are shown, splitting patterns exhibit a mix of trench-parallel, trench-perpendicular, and oblique fast directions. Figure reproduced from Long [2013].

Finally, subduction trenches on Earth are distinctively curved and form arcuate shapes (see Figure 1). Narrow subduction zones have a single-arc trench geometry (e.g., South Sandwich), while trenches of wide subduction zones tend to form a multiple-arc geometry (e.g., South America). In the latter case, toward the mantle wedge concave, wide trench segments are connected via narrow convex intersections.

The flow of mantle material in the vicinity of subduction zones is mostly controlled by the sinking portions of the surface plates. Measurements of shear wave splitting provide some insight into the general flow directions in or beneath mantle wedges on present-day Earth as compiled by Long [2013] and shown in Figure 1. Trench-parallel fast directions are generally observed beneath the wedge (i.e., in or behind the slab) and attributed to trench-parallel back-slab mantle flow. Trench-parallel fast directions are also observed in the mantle wedge close to the slab and often become trench perpendicular in the back arc farther away from the slab. In contrast, current geodynamic models do not agree with the prediction of trench-parallel flow in the back of slabs made by observations of seismic anisotropy.

Subduction-induced flow has been studied extensively with 2-D models in which the trench was either artificially fixed [e.g., Davies and Stevenson, 1992; van Keken, 2003], artificially moved [e.g., Davies, 1995; Garfunkel et al., 1986; Christensen, 1996], or could freely evolve [e.g., Gurnis and Hager, 1988; Becker et al., 1999; Enns et al., 2005]. This led to a robust understanding of the 2-D poloidal flow behind and in front of the sinking slab. More elaborate numerical models that incorporate the third dimension were performed only recently [e.g., Stegman et al., 2006; van Heck and Tackley, 2008; Cramer et al., 2012a]. These models are able to produce not only poloidal but also toroidal motions. Moreover, Stegman et al. [2006] showed that most (~69%) of the gravitational energy arising from the negative buoyancy of the slab is converted into toroidal motion and another ~13% into mantle flow parallel to slab displacement. They further showed that the fastest trench retreat is observed for trench width of around 600 km. Subduction trench width on Earth is strongly variable and ranges from 200 km (e.g., the Calabrian slab) to more than 5000 km (e.g., the Nazca slab). A clear compilation of trench width, plate boundaries, and plate velocities is given by Schellart and Rawlinson [2010].

Three-dimensional analogue laboratory experiments were performed both early on [e.g., Kincaid and Olson, 1987] and also more recently [e.g., Funicello et al., 2003; Schellart, 2004; Bellahsen et al., 2005]. These studies provide important insights into the 3-D complexity of mantle flow that is produced by laterally discontinuous slabs.

The main focus of this study is to understand the dynamic implications of 4-D (i.e., three spatial dimensions plus time) self-consistent subduction in a global context, in which the system is less constrained than in the studies reviewed above. Behavior such as the spontaneous development of subduction trench and slab curvature, trench migration, and subduction-induced mantle flow are of particular interest. To obtain realistic behavior, it is necessary for subduction to be single sided as observed on Earth, in contrast to the double-sided subduction typically obtained in mantle convection models with self-consistent plate tectonics [e.g., *Tackley, 2000; van Heck and Tackley, 2008; Foley and Becker, 2009; Nakagawa et al., 2010*], although the presence of continents can be helpful in this regard [*Rolf and Tackley, 2011*]. Obtaining single-sided subduction was recently found to require both a free surface *Crameri et al., 2012a; Schmeling et al., 2008* and a weak lubricating crustal layer between the subducting slab and overlying plate [*Gerya et al., 2008*]. Here we use a global, dynamically self-consistent model of mantle convection in both Cartesian and fully spherical geometry that produces single-sided subduction, thanks to these ingredients of a free surface and a weak, hydrated crustal layer [*Crameri et al., 2012a*].

2. Model and Method

The model used for this study is intended to produce time-dependent 3-D, global mantle convection and plate tectonics in a dynamically self-consistent way. The experiments are, therefore, calculated in a larger domain than regional studies: either a 3-D Cartesian domain (with an aspect ratio $x:y:z$ of 4:4:1) or a 3-D full spherical shell. The model assumes the Boussinesq approximation, and the rheology is strongly temperature and pressure dependent:

$$\eta(T, p) = \eta_0 \cdot \exp \left[\frac{E_{\text{act}} + pV_{\text{act}}}{RT} \right] \quad (1)$$

where η is the viscosity, p is the pressure, $R = 8.314 \text{ J mol}^{-1} \text{ K}^{-1}$ is the gas constant, T is the temperature, $E_{\text{act}} = 240 \text{ kJ/mol}$ the activation energy, $V_{\text{act}} = 8.89 \times 10^{-7} \text{ m}^3 \text{ mol}$ the activation volume, and η_0 is set such that η is the reference viscosity at $T = 1600 \text{ K}$ and $p = 0 \text{ Pa}$. A Rayleigh number of 10^6 is used, and the model is purely internally heated. Additionally, plastic yielding is included using a Drucker-Prager yield criterion with the pressure-dependent yield stress σ_{yield} based on Byerlee's law:

$$\sigma_{y,\text{brittle}} = C + p\mu \quad (2)$$

with specified friction coefficient μ and a cohesion C of 10 MPa. Finally, the viscosity is limited to 9 orders of magnitude by applying an upper and a lower cutoff of $\eta_{\text{max}} = 10^5 \eta_0$ and $\eta_{\text{min}} = 10^{-4} \eta_0$ (see Table 1).

A crustal layer is added in some calculations. If applied, it has a 2 orders of magnitude lower viscosity and yield stress compared to mantle material and is assumed to become weak crust after it has resided in the top $d_{\text{crust}} = 15 \text{ km}$ of the solid Earth for a time period of $t > 25 \text{ ka}$. It is converted to regular mantle again when subducted below a depth of $d > 900 \text{ km}$ into the mantle. The outer boundary is isothermal (300 K) and mechanically a free surface. The bottom (core-mantle) boundary is free slip and has zero heat flux. In Cartesian geometry the side boundaries are periodic.

Calculations are performed using the code StagYY [*Tackley, 2008*], which is based on a finite-volume discretization and a multigrid flow solver. Nondiffusive tracers track the different compositions (in this case regular mantle, sticky air, and weak crust). The model domain consists of the whole mantle depth plus a "sticky-air" layer on top [*Matsumoto and Tomoda, 1983; Schmeling et al., 2008*], which is a good approach for simulating a free surface in an Eulerian grid and consists of low-viscosity "air" layer of (nearly) zero density that decouples the surface of the lithosphere from the top of the model domain. For a good free-surface treatment this air layer has to (a) be sufficiently thick and (b) have sufficiently low viscosity [*Crameri et al., 2012b*]. Using the actual viscosity of air or water viscosity is computationally unfeasible, but the application of the test conditions provided in *Crameri et al. [2012b]* show that the sticky-air viscosity assumed here is sufficiently low in combination with the layer thickness to properly allow changes in topography that are driven by mantle convection.

Some of the large-scale data presented in this study are visualized using the visualization software VisIt [*Childs et al., 2005*].

Table 1. Parameters Used in This Study

Parameter	Symbol	Nondimensional	Dimensional	Units
		Value	Value	
Reference viscosity	η_0	1	10^{23}	Pa s
Mantle depth	D	1	2890	km
Gravitational acceleration	g	-	9.81	m s^{-1}
Thermal conductivity	k	-	3	$\text{W m}^{-1}\text{K}^{-1}$
Thermal diffusivity	κ	1	10^{-6}	$\text{m}^2 \text{s}^{-1}$
Thermal expansivity	α	-	3×10^{-5}	K^{-1}
Temperature gradient	ΔT	-	2500	K
Reference density	ρ_0	-	3300	kg m^{-3}
Heat capacity	$C\rho_0$	-	1200	$\text{J kg}^{-1}\text{K}^{-1}$
Internal heating rate	H	20	5.44×10^{-12}	W kg^{-1}
Activation energy	E_{act}	11.55	240	kJ mol^{-1}
Activation volume	V_{act}	4.0	8.8878×10^{-7}	$\text{m}^3 \text{mol}$
Friction coefficient	μ	0.07 ^a	-	-
Cohesion	C	100	6.3410^5	Pa
Upper viscosity cutoff	η_{max}	$10^5 \eta_0$	10^{28}	Pa s
Lower viscosity cutoff	η_{min}	$10^{-4} \eta_0$	10^{19}	Pa s
<i>Stick-air layer^b</i>				
Thickness	d_{st}	0.05	145	km
Viscosity	η_{st}	$10^{-2} \eta_0$	10^{21}	Pa s
<i>Weak crustal layer^b</i>				
Thickness	d_{crust}	0.005	15.2	km
Viscosity	η_{crust}	$10^{-2} \eta_0$	10^{21}	Pa s
Friction coefficient	μ_{crust}	$10^{-2} \mu$	-	-
Cohesion	C_{crust}	100	6.34×10^5	Pa

^aIndicated is standard setup. Parameter variation is mentioned separately.

^bIf applied.

2.1. Initial Conditions

In this study we present experiments using different initial conditions in both Cartesian and spherical model domains as explained below (see Table 2). Here we do not aim to study the onset of subduction, so all initial configurations contain preexisting slabs, which are idealized and initially vertical in order to not bias the system toward single-sided subduction.

2.1.1. Cartesian Domain

Cartesian models contain a single, straight, vertical initial slab in the middle of the domain. The two Cartesian initial conditions differ only in the lateral extent of the slab. The first initial setup includes a finite-width slab that spans 2/3 of the domain width; i.e., the slab is 8000 km long. The second Cartesian initial setup has a slab that spans the full domain width, which due to periodic side boundaries, is an infinitely extending slab. The lithosphere is also divided by an initial spreading ridge striking along one side boundary of the domain, parallel to and at a distance of 6000 km from the subduction zone, by reducing the cold thermal boundary layer thickness to zero. The boundary layer thickness w_{BL} increases in both directions away from the spreading center toward the subduction zone according to the standard $\sqrt{\text{age}}$ law

$$w_{\text{BL}}(x) = w_{\text{BL},0} \cdot \sqrt{\Delta x_{\text{sc}}} \tag{3}$$

where $w_{\text{BL},0}$ is a constant controlling the maximum thickness of the plate, x is the horizontal coordinate, and Δx_{sc} is the distance from the spreading center at any given position x . This is done to support the negatively buoyant slab by reducing resistance against horizontal plate motion at the beginning of the experiment.

Table 2. Model Setups Presented in This Study

Tag	Box Geometry	Initial Condition	Aspect Ratio ($x : y : z$)	Resolution ($n_x \times n_y \times n_z \times n_b$)	Friction Coefficient (μ)	Weak Crustal Layer
Case1	Cartesian	partial width slab	4:4:1	$256 \times 256 \times 64$	0.07	yes
Case2	Cartesian	full width slab	4:4:1	$256 \times 256 \times 64$	0.07	yes
Case3	Spherical	partial width slab	global	$128 \times 384 \times 64 \times 2$	0.09	no

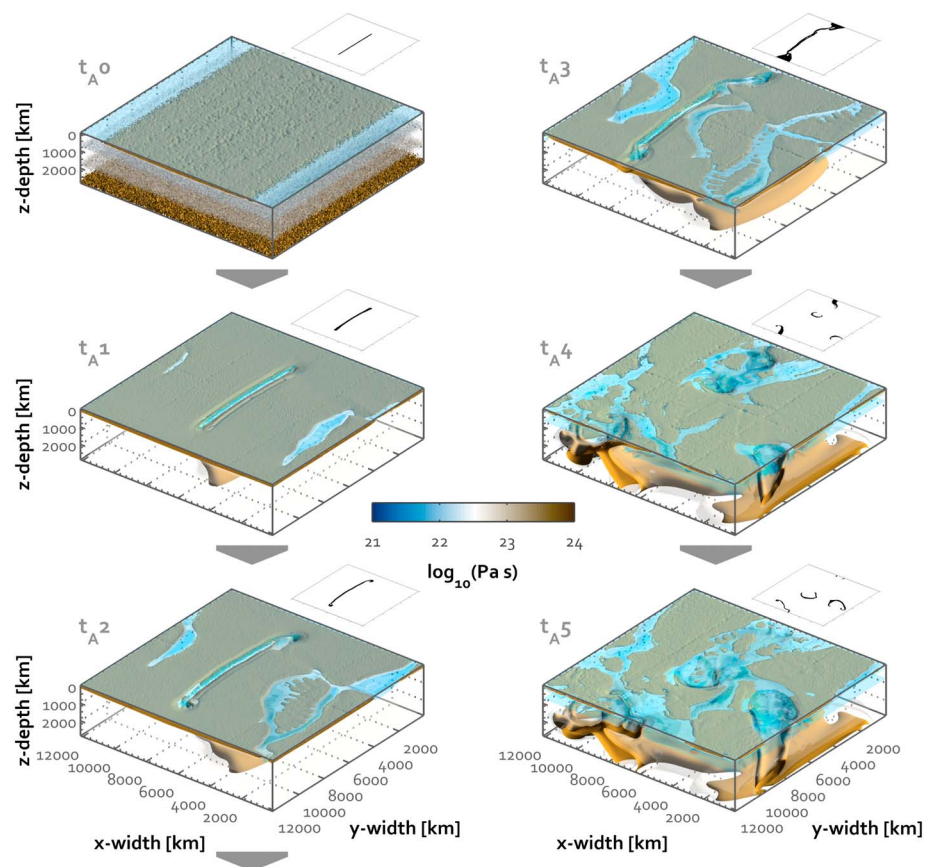


Figure 2. Time evolution of a Cartesian experiment with an initial finite-width slab shown by viscosity isosurfaces that represent the strong core of the plates (brown) and the low viscosity of the sticky air and plate boundaries (transparent blue). Time snapshots are taken at times t_{A0} , t_{A1} , t_{A2} , t_{A3} , t_{A4} , and t_{A5} , which are further described in Table 3. Small plots show the position of the subduction zones (black) at the surface.

In order to prevent a perfectly symmetric setup, a small and random initial temperature perturbation of (± 125 K) is applied on the whole model domain (except for the sticky-air layer).

2.1.2. Spherical Domain

The spherical initial condition also assumes a mobile lid and ongoing subduction: a symmetric, finite-width slab is placed along half of the Yin-Yang grid boundary, which thus limits its width. The plate thickness is constant in both initial setups and defined by $w_{BL}(x) = w_{BL,0}$.

3. Results and Discussion: Cartesian Geometry

In order to model and investigate the development of Earth-like trench curvature, it is best to start by considering a model with an initially straight trench. Due to its geometry, a Cartesian model is, therefore, the most suitable choice.

3.1. Time Evolution of an Initial Finite-Width Slab

The first three-dimensional Cartesian model that is presented here (i.e., case1) assumes a finite-width initial slab, as defined in section 2.1. Its time evolution is shown in Figure 2, and the corresponding time tags (t_{A0} – t_{A5}) are explained in Table 3.

The experiment starts at t_{A0} with the initial, symmetric, ~ 8000 km long slab placed in the middle of the domain and the initial spreading ridge along one side boundary of the domain. At t_{A1} the model starts to develop asymmetric (but still partially double sided) subduction and a slight curvature in the subduction trench. The portions of the plate normal to the trench exhibit a drag toward it, causing extension that maintains the spreading ridge at these locations. The ridge spontaneously forms two segments that have

Table 3. Time Table of Snapshots Shown in Figures

Case Tag	Time Tag	Nondimensional Time	Dimensional Time (Ga) ^a	Figure
Case1	t_{A0}	0	0	Figure 2
"	t_{A1}	2×10^{-3}	0.772	Figure 2
"	t_{A2}	2.49×10^{-3}	0.964	Figure 2
"	t_{A3}	2.98×10^{-3}	1.15	Figures 2 and 4
"	t_{A4}	4.21×10^{-3}	1.63	Figure 2
"	t_{A5}	4.44×10^{-3}	1.72	Figures 2 and 4
Case2	t_{B0}	0	0	Figure 3
"	t_{B1}	3.02×10^{-3}	1.17	Figure 3
"	t_{B2}	3.18×10^{-3}	1.23	Figure 3
"	t_{B3}	3.44×10^{-3}	1.33	Figures 3 and 5
"	t_{B4}	3.61×10^{-3}	1.4	Figure 3
"	$t_{B4-t_{B5}}$	4.28×10^{-3}	1.65	Figure 5
"	t_{B5}	4.72×10^{-3}	1.83	Figure 3
Case3	t_{C0}	0	0	Figure 8
"	t_{C1}	2.83×10^{-3}	1.09	Figure 8
"	t_{C2}	3.89×10^{-3}	1.5	Figure 8
"	t_{C3}	4.59×10^{-3}	1.78	Figure 8
"	t_{C4}	5.31×10^{-3}	2.05	Figure 8
"	t_{C5}	6.25×10^{-3}	2.42	Figure 8

^aDimensionalized using the diffusion time scale $t_{\text{diff}} = \frac{D^2}{\kappa}$, where D is the model depth and κ is the thermal diffusivity.

an offset of about 1000 km. Extensions of the ridge farther away along its strike, however, do not experience large extension and thus close. This more prominent ridge at $x \approx 2000$ km opens further and develops a microplate bounded by two ridges at t_{A2} . The narrow ridge on the subducting plate also spreads farther, while the subduction zone still has a slight curvature and propagates toward the side boundaries of the box along its strike direction. It reaches the boundary (that is also its other end) at t_{A3} . More complicated double and triple spreading centers form and move toward the subduction trench. The arrival and subduction of the spreading ridges shut off most of the subduction at t_{A4} .

The collision of the spreading ridge with the subduction trench causes surface plate portions to detach from the double-sided slab. This leads to upper plate portions that are no longer subducting. After the detachment of one of the two colliding plates from the sinking plate portion, a few smaller parts (all originating from the former subduction zone), however, continue to subduct, now single sidedly. They, therefore, develop strong trench curvature that leads to the characteristic arcuate shape of subduction zones as also observed on Earth. Due to the small width extent, these subduction zones develop a high trench retreat velocity of up to 10 cm/a (compared to the characteristic subduction-plate velocity of around 3 cm/a). After propagating throughout the whole domain at t_{A5} , subduction eventually shuts off.

3.2. Time Evolution of an Initial Infinitely Extending Slab

The time evolution of a 3-D Cartesian model with an initial 2-D (i.e., infinitely extending) slab (i.e., case2) is shown in Figure 3. The corresponding time tags (t_{B0} – t_{B5}) are explained in Table 3.

The snapshot at t_{B0} shows the initial state of the experiment with an initial slab (in the middle of the domain) and an initial spreading center (at the domain side boundary). Double-sided subduction characterizes the initial phase; however, the spreading is not perfectly symmetric, which displaces the spreading ridge toward the trench (between t_{B0} and t_{B1}). Due to this convergent motion and the resulting plate extension, the ridge stays intact but gets laterally displaced by the formation of a ~ 1000 km long transform offset. Shortly thereafter, asymmetric, single-sided subduction evolves, with the spreading ridge situated on the overriding plate portion (which is also connected via the wrap-around boundaries to the subducting portion) (t_{B1}). At t_{B2} a new, similarly displaced ridge forms on the subducting plate portion due to ongoing convergence (the subduction-plate velocity is around 1 cm/a). It is also offset by a ~ 1000 km long transform area (see section 3.5 for more details). The trench portion that is closest to the arriving ridge thereby develops the strongest curvature due to a regionally faster trench retreat with a velocity of around 2 cm/a. The

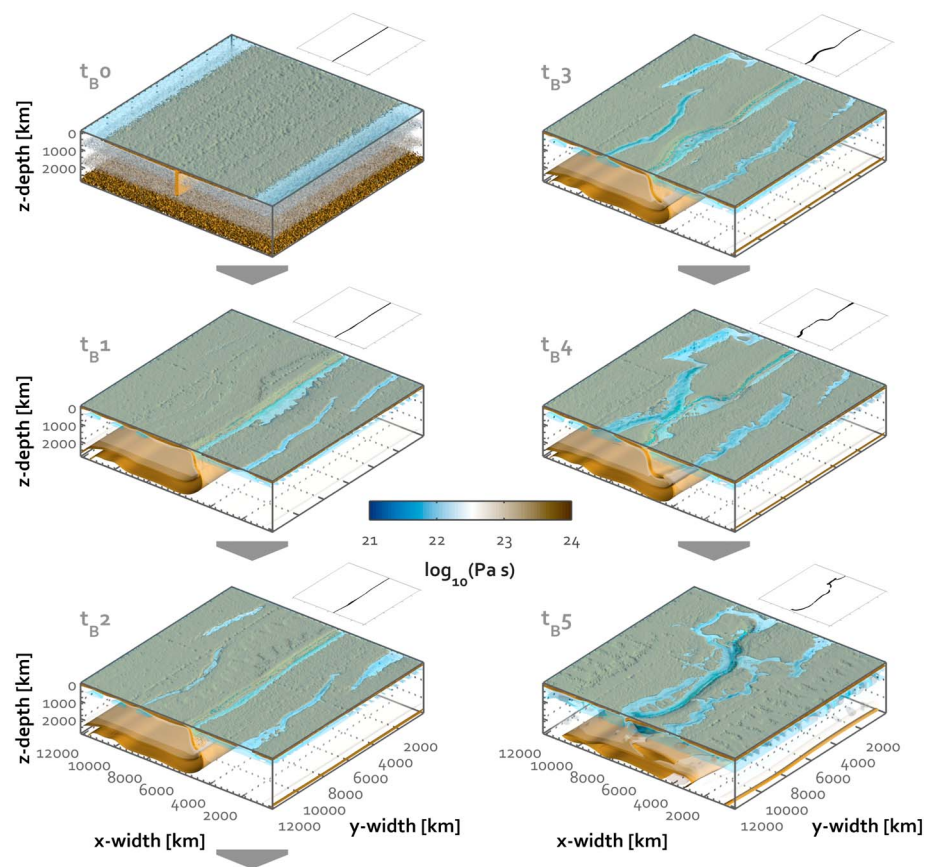


Figure 3. Time evolution of a Cartesian experiment with an initial 2-D (i.e., infinitely extending) slab shown by viscosity isosurfaces that represent the strong core of the plates (brown) and the low viscosity of the sticky air and plate boundaries (transparent blue). Time snapshots are taken at times t_{B0} , t_{B1} , t_{B2} , t_{B3} , t_{B4} , and t_{B5} , which are further described in Table 3. Small plots show the position of the subduction zones (black) at the surface.

experiment spontaneously develops curvature at the subduction trench at t_{B3} . Ridge subduction begins to occur at t_{B4} and gives rise to more complicated dynamics that results in a subduction-polarity reversal along most of the trench at t_{B5} . Only a narrow portion of the subduction zone does not flip polarity. This leads to a lateral detachment and a subsequent autonomous and short-lived evolution of a second subduction system. On the remaining part, a double-arcuate shaped subduction zone evolves until a final shut-off of the mobile lid.

3.3. Subduction Zone Dynamics

Figure 4a shows vertical slices through the model domain for the case with an initially finite-width slab (i.e., case1) at time t_A3 . While a major part of the subduction zone is still double sided, part of it has already evolved to single sided at $y = 3000$ km. This single-sided part of the subduction trench also develops a strong spontaneous curvature. The onset of single-sided subduction from initially double-sided subduction requires one of the two colliding plates to detach from its sinking slab. Such a lithosphere-scale failure requires a strong strength difference between one colliding plate and its opposite. As in nature (and in models employing a free surface), a more distributed bending at the subduction zone due to a forebulge and a deep trench increases a plate's strength [Cramer *et al.*, 2012a]. If, additionally, a weak plate portion on one of the two plates enters a subduction zone (e.g., due to a ridge-trench collision), a large strength difference results and therefore causes the weaker plate to break. Once a plate subducts single sidedly, the strength difference that is needed to prevent both plates from sticking together is maintained by the strongly deformed and hence weak subduction channel (i.e., the preset weak crustal layer in the models presented here).

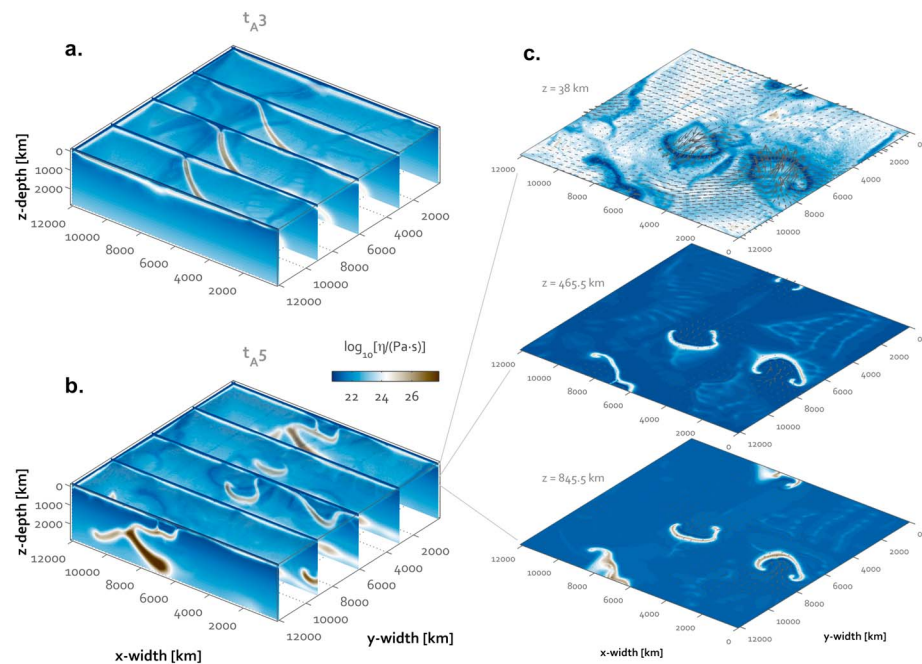


Figure 4. (a, b) Vertical slices through 3-D viscosity field of a developed Cartesian experiment (case1) with an initial finite-width slab setup at times t_{A3} in Figure 4a and t_{A5} in Figure 4b. Vertical slices are overlain by a transparent horizontal slice through the lithosphere. (c) Horizontal slices through 3-D viscosity field of the experiment shown in Figure 4b at time t_{A5} . Horizontal slices are overlain by velocity arrows.

Figures 4b and 4c show the viscosity at a later stage (t_{A5}) in vertical cross sections and in horizontal slices, respectively. Visible in vertical cross sections is a complicated slab pattern that resulted from former double-sided subduction, slab break off, and a small and continuing subduction zone. Single-sided subduction and narrow slabs are now predominant and visible, for example, in the cross section at $y = 6000$ km, where two separate, adjacent subduction trenches move past each other in opposite directions. Slab structures resembling two adjacent slabs that are merged at depth (thus forming a “u”-shape) in cross section indicate a single subduction zone that simply evolves in three dimensions (i.e., also normal to the cross section), as can be seen in horizontal slices (Figure 4c). Also visible in horizontal slices are narrow plate boundaries and more or less rigid plates. The subducting plate portions are often stable in their position (i.e., they do not move) in the reference frame defined by zero net rotation. The smaller overriding plates move fastest (toward the trench) to accommodate the fast trench retreat of the narrow subduction zones present at this stage. Deeper in the mantle, the highest horizontal velocities are observed in the same regions: progressing slabs force mantle material to move around their edges and into their arc structure.

As mentioned, the initial subduction zone evolves differently at different positions along the trench, as in the experiment with an infinitely wide initial slab (i.e., case2) shown in Figure 5a. The subducting plate moves fastest at about $y = 9000$ km; and thus, three major features are distinct at this location compared to other positions along the strike of the subduction zone: (i) faster trench retreat is observed in this area resulting in a flatter dipping slab; (ii) the spreading ridge in the subducting plate is closer, and thus, the plate age is younger at the trench; and (iii) a new ridge is forming, accompanied by spreading in the overriding plate close to the trench. After some time (at t_{B4} – t_{B5}), the ridge on the subducting plate arrives at the subduction zone. As a result of the trench-ridge collision, subduction stops on most parts due to slab break off. At these parts of the trench, the overriding plate starts to subduct and produces a subduction-polarity reversal between t_{B3} and t_{B4} (see Figure 5b and *Cramer* [2013, Chapter 3] for more details). An exception is observed at $y = 3000$ km, where a small portion of the subduction zone maintains the former subduction direction and subsequently evolves in the opposite direction.

Faster subduction relative to an approaching ridge can be attributed to three changes in forcing on the plate: (i) The driving ridge push force is distributed over a smaller area (due to the small total size of the subducting plate) and thus experienced by the plate as being stronger. (ii) The opposing basal drag on

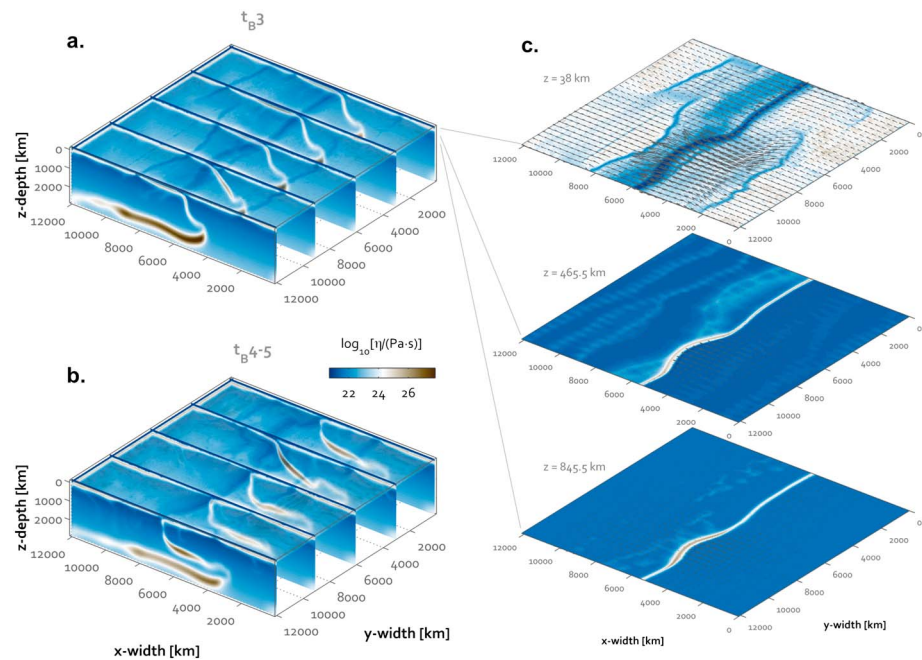


Figure 5. (a, b) Vertical slices through 3-D viscosity field of a developed Cartesian experiment (case2) with an initial 2-D (i.e., infinitely extending) slab setup at times t_{B3} in Figure 5a and $t_{B4}-t_{B5}$ in Figure 5b. Vertical slices are overlain by a transparent horizontal slice through the lithosphere. (c) Horizontal slices through 3-D viscosity field of the experiment shown in Figure 5a at time t_{B3} . Horizontal slices are overlain by velocity arrows.

the plate decreases with decreasing plate area. (iii) The opposing bending force in the slab hinge is smaller due to a younger and thus warmer and thinner plate.

The faster subduction accompanied by faster trench retreat leads to extension and finally rifting in the upper plate. The heterogeneous trench retreat velocity along the trench strike is responsible for spontaneously forming a trench curvature of about 5000 km width at the time shown in Figure 5a.

3.4. Trench Curvature and Mantle Flow

Trench curvature arises spontaneously from an initial straight trench. Figure 5c shows the model with an initial infinitely extending slab at a time (i.e., t_{B3}) when the trench starts to spontaneously develop curvature. The motion at the surface is nearly constant and in the same directions for the different plate portions. These approximately rigid plate portions are bounded by either a subduction zone, a spreading ridge, or a more diffuse transform feature. The approach of a curved spreading ridge (at $x = 8000$ km and 12000 km $> y > 5000$ km) induces an oppositely directed curvature of the trench. The locally faster trench retreat caused by this curvature subsequently forces the adjacent plate (on the inside of the arc) to move faster toward the trench. This happens on about half of the model width and thus causes the formation of a spreading ridge that also only extends over half the model width.

Deeper in the mantle, the highest velocities are again in roughly the same regions as they are at the surface: The developing slab curvature causes mantle material to flow normally into the forming arc. Once these arcs are fully developed, they can separate from the rest of the subduction zone and evolve as separate features, as, for example, in the model case1 (see Figure 4c). Wide subduction zones (as the one of case2) can additionally produce two or more arcs that are connected by narrow, oppositely curved kinks as is occurring in Figure 3 at t_{B5} , or more clearly visible in spherical geometry (see section 4). These multiple arcs are formed when the mantle material cannot reach the far edge of the slab but instead accumulates in the middle of the slab. It cannot just rest there but starts to push the retreating slab from behind causing a slow down (or maybe an advance) of the slab in this particular region. If this accumulation continues, it can lead to “slab tunneling” by inducing local flat subduction, as further discussed in section 4.5.

3.4.1. Interaction Between Trench Curvature and Mantle Flow

Trench displacement and the inclined sinking of slabs cause the mantle in the vicinity to adjust. Mantle flow induced by subduction can be decomposed into 2-D poloidal flow in the mantle wedge and behind the

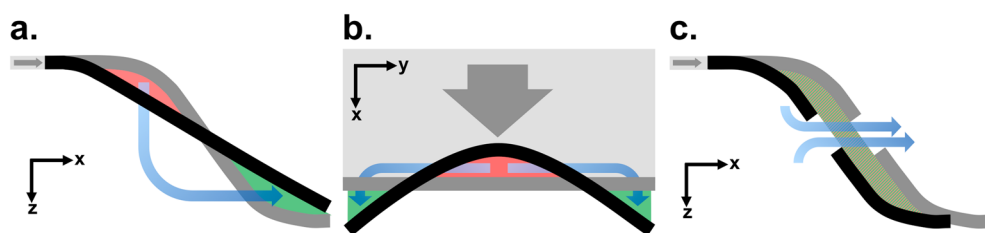


Figure 6. Sketch of three different ways to produce fast subduction trench retreat that are (a) flattening of the slab from side view, (b) curvature of the slab from top view, and (c) partial slab damage (i.e., slab window) from side view. Shown are initial (grey) and end position (black) of the plate and according mantle flow (blue) that displace mantle material from its initial region (red) to its final region (green).

subduction zone, and 3-D toroidal flow around slab edges [Stegman *et al.*, 2006]. The latter is mainly responsible for the horizontal displacement of mantle material and is the most efficient way of allowing the slab to retreat. Since the whole mantle portion behind a slab has to escape to the other side, it is easiest for the slab to retreat in the central parts than at the edges. This, therefore, leads to deformation of the slab and the trench above, usually into the characteristic arcuate shape.

Trench curvature is controlled by the competition between the trench's tendency to retreat and the mantle's opposition to being displaced. Fast retreat cannot happen over the whole width of the subduction zone because it would require the whole mantle to be displaced backward. However, fast retreat is enabled by a simple mantle displacement under either of the following three conditions:

1. The slab flattens and allows mantle material that is displaced downward by trench retreat at shallow depth to sink and fill the space created by the flattening of the slab (Figure 6a).
2. The mantle material that is displaced can escape laterally to one or both sides where fast slab retreat thus becomes disabled (Figure 6b). This creates an arcuate curvature of the slab.
3. The mantle material that is displaced can escape through a partially damaged slab (i.e., a slab window) (Figure 6c).

Conditions 1 and 2 might both contribute simultaneously to fast trench retreat in the presence of an intact slab.

The highest velocities in the model are observed to be linked to horizontal toroidal mantle flow. This finding supports previous studies suggesting that most of the slab's potential energy is converted into mantle flow [Forsyth and Uyeda, 1975; Stegman *et al.*, 2006; Capitanio *et al.*, 2007, 2009], rather than in bending of the slab itself as other studies suggest [Houseman and Gubbins, 1997; Becker *et al.*, 1999; Funicello *et al.*, 2003; Bellahsen *et al.*, 2005]. The partitioning between these two energy sinks is believed to be strongly related to the magnitude of the slab bending radius and the effective viscosity ratio between slab and ambient mantle.

3.4.2. Comparison to Observations

Subducting slabs and associated trenches spontaneously develop arcuate shapes in both modeled geometries (see also section 4); in fact, an arcuate geometry is the natural form into which subduction zones tend to evolve. Spontaneous subduction trench curvature in these experiments is triggered by heterogeneities within the lithosphere. An approaching spreading ridge that is curved or offset along its strike is one such heterogeneity, causing the subduction zone to deform on the horizontal plane. A prerequisite for nature-like, arcuate trench curvature is asymmetric single-sided subduction.

The curvature varies strongly both in the models presented here and on Earth (see Figure 1). On Earth, most subduction zones are strongly influenced by adjacent continental lithosphere. Even so, there is still a clear pattern of arcuate trench geometry at most ocean-continent collision zones, for example, the double-arc geometry of the wide subduction system at the West Coast of South America: A first arc extends along the Colombia and the Peru subduction zone until it reaches the kink at the Bolivia subduction zone. The Chile subduction zone farther south then makes up the second (although less curved) arc.

Apart from the ocean-continent collision zones, there are a few examples of ocean-ocean subduction that are not directly influenced by adjacent continents and have a typical arcuate shape. Examples are the Mariana subduction zone in the East Pacific or the South Sandwich subduction zone in the Southern

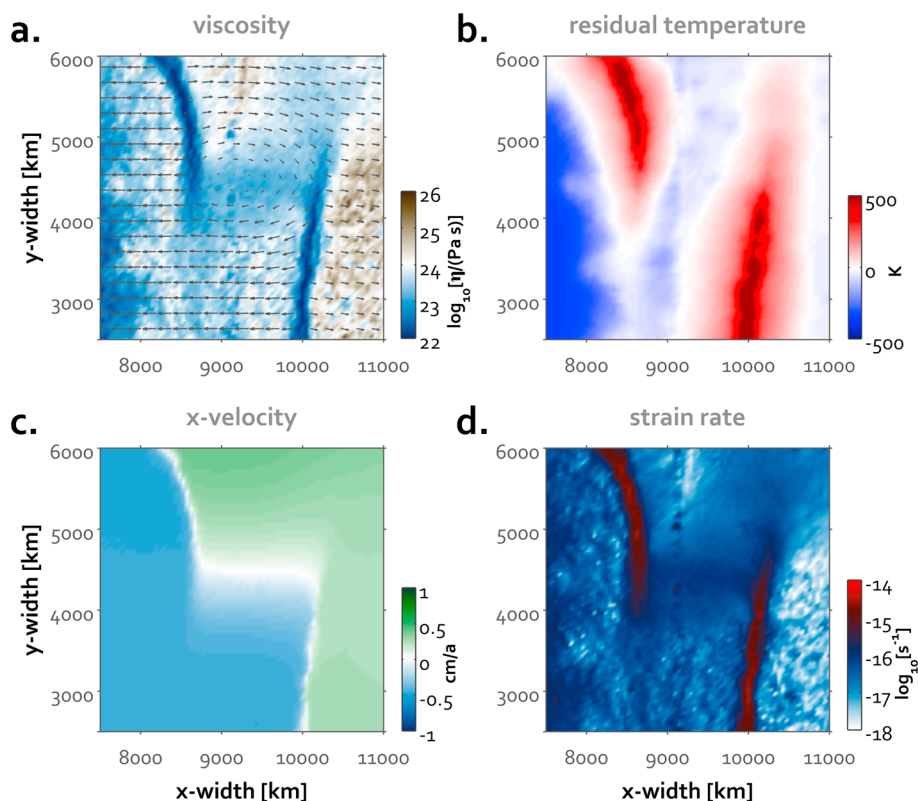


Figure 7. Close up of a horizontal slice at $z = 38$ km through a 3-D Cartesian experiment (case2) at time t_{g3} showing (a) viscosity overlain by velocity arrows, (b) residual temperature of the full model extend horizontal average, (c) x velocity, and (d) strain rate.

Atlantic. Thus, observations strongly suggest—in agreement with the modeling results—that an arcuate slab geometry is the natural form and straight subduction zones tend to decay into this.

A complicating factor in the actual Earth that is not included here is the boundary between the upper mantle and lower mantle, at which an endothermic phase transition and likely viscosity increase occur. In the models presented here a faster trench retreat simply yields a shallower slab. On Earth, however, the combination of fast retreat and the above mentioned factors tends to cause a draping of the slab on top of the upper-lower mantle transition at ~ 670 km depth [e.g., *Zhong and Gurnis, 1995; Christensen, 1996*]. Fast-retreating subduction zones might, therefore, favor slab stagnation on the 670 km discontinuity, while slower retreating trenches might favor a slab penetration into the lower mantle.

3.5. Spreading Centers and Transform Features

The occurrence of destructive (convergent) plate boundaries always implies the occurrence of constructive (divergent) plate boundaries. The spreading ridges obtained in the models presented here are narrow features. Their visualization in Figures 2 and 3 is, therefore, somewhat misleading. The young plate region around these features is weak, and the actual ridge, therefore, appears wider when plotting viscosity isosurfaces. The velocity field normal to the ridge axis, in contrast, shows oppositely directed plate velocities that are offset by only a few tens of kilometers (Figures 5c and 7c). Also, the strain is localized mostly within these narrow zones (Figure 7d). Strong lateral temperature variations occur in the model in these regions: of the order of 1000 K over about 1000 km (Figure 7b). The two adjacent spreading ridges overlap in their strike direction for around 1000 km.

An interesting feature that occurs in combination with rifting is the spontaneous development of ridge offsets. As can be observed in Figure 3, spreading centers develop at least a double-ridge or sometimes a triple-ridge offset. These ridge offsets between adjacent portions are typically around 1000–2000 km.

The connected portions of the ridge further develop curvature that sometimes results in a transform fault connecting the newly created, offset portions of it.

The occurrence of laterally displaced rifting is always accompanied by the third kind of plate boundary, namely transform faults. These conservative plate boundaries accommodate oppositely directed plate motions in the segments between two adjacent spreading ridges. To obtain natural looking, narrow transform faults in global models of mantle convection is still challenging and might require an efficient weakening mechanism [e.g., *Bercovici and Ricard, 2005*]. Nevertheless, strong strike-slip motion can be observed in the present experiments, although it is distributed laterally over a wider region of around 500 km (Figures 7c and 7d). There is no narrow fault or shear zone to take up all the deformation; and thus, such features are not visible in the temperature field (Figure 7b).

The transform features connect the ridge segments in a roughly 90° angle toward the strike of the ridges, as is seen in more realistic regional rifting models [*Gerya, 2012*] and in nature [*DeMets et al., 2010*].

3.5.1. Comparison to Observations

The presented models naturally develop spreading ridges, which are offset by transform faults. Two characteristics of the obtained transform faults are not, however, fully realistic. First, the obtained ridge offsets are around 1000 km, which is larger than the majority of offsets observed on Earth [*DeMets et al., 2010*] or obtained in regional modeling [*Gerya, 2012*] although there are a few examples of such large ridge offsets in nature; in particular, the Charlie-Gibbs fracture zone, which offsets the northern and southern parts of the Atlantic ridge by about 1000 km and can be traced for more than 2000 km. Second, the model transform zones are much wider (more diffuse) than the faults observed in nature. This is because there is no strain weakening or strain rate weakening mechanism in our model to create the positive feedback that leads to such features; idealized models of global flow [e.g., *Bercovici, 1995; Tackley, 1998*] or more realistic models of spreading centers [*Gerya, 2012*] show that such feedback is necessary for forming localized transform faults.

Despite being quite broad in our presented models, it still appears to be efficient enough (from the perspective of global convection) for transform faults to accommodate the lateral shearing in wide, viscously deforming zones instead of rupture along a very narrow and weak fault. The spreading centers obtained in the models presented here are remarkably stationary features.

4. Results and Discussion: Spherical Geometry

Spherical geometry has the advantage of correctly reproducing the aspect ratio of Earth's mantle and also results in lateral "squeezing" with increasing depth, i.e., the surface area decreases with depth, which might encourage curved subduction zones. The appropriate aspect ratio of the mantle in spherical models thus allows us to study the evolution of a mobile lid in a more natural environment.

4.1. Time Evolution of an Initial Finite-Width Slab

A three-dimensional spherical experiment started by a finite-width (but curved) initial slab (as defined in section 2.1) is shown in Figure 8. The asymmetric global initial slab distribution causes a slight heterogeneity in the lithosphere at t_c0 . As soon as the initial, double-sided slab starts to tilt, it immediately develops single-sided subduction operating in different directions on different locations along the former slab width. This causes the different portions of the slab to break apart and evolve separately. Independent of their width, all segments start to form typical arcuate curvature at t_c1 . The sublithospheric mantle flow is already dominated by the motions of the sinking plate portions. At t_c2 , spreading ridges that are curved and often offset occur inside all the arcs of the developing subduction zones. As the subduction trenches develop (mostly by retreating at around 2 cm/a) at t_c3 , they create more complex patterns of spreading ridges that often have straight and laterally offset segments. At t_c4 , the subduction zones collide and merge, partially shut off or continue to evolve throughout the model. About one quarter of the sphere has no active downwelling. Major hot upwellings are, therefore, preferentially located in this area underneath the intact portion of the lid (not shown). Subduction zones and spreading ridges evolve farther, forming more complex and mostly connected patterns of plate boundaries at t_c5 . The former build multiple-arc zones of subduction and the latter straight ridges that are slightly perpendicularly offset and sometimes interconnect forming triple junctions. In contrast to subduction zones, these spreading centers are surprisingly stable in terms of their position throughout the model.

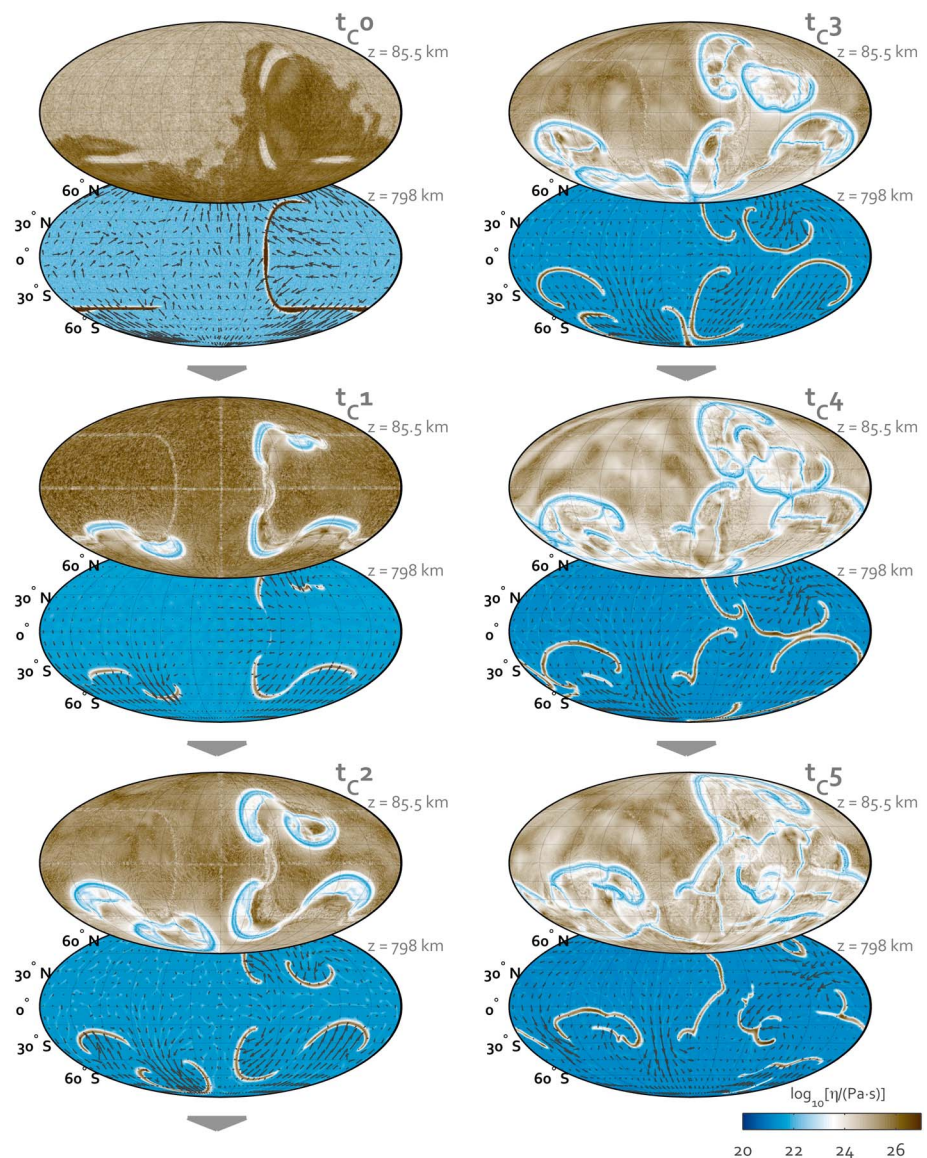


Figure 8. Time evolution of a global spherical experiment (case3) with an initial finite-width slab setup shown by horizontal slides of the viscosity field at 85 km (top subplot) and 800 km (bottom subplot) depth. Time snapshots are taken at times t_{C0} , t_{C1} , t_{C2} , t_{C3} , t_{C4} , and t_{C5} , which are further described in Table 3.

4.2. Slab Tearing

Tectonic reconstructions and present-day observations indicate that after a subduction zone starts and evolves through time, it might end by failure and detachment of the subducted plate portion [e.g., *Nemcok et al.*, 1998; *Stampfli and Borel*, 2002]: A well-developed subduction zone might evolve into an arc-continent collision, a continent-continent collision or an obduction, or it might evolve into another state that causes the subducting plate to resist the driving forces of subduction. Such scenarios are suggested to happen on present-day Earth, for example, in the Mediterranean region [e.g., *Wortel and Spakman*, 2000], and are successfully reproduced by laboratory modeling [e.g., *Chemenda et al.*, 2000; *Regard et al.*, 2005] and numerical modeling [e.g., *Burkett and Billen*, 2009, 2010; *Duretz et al.*, 2012; *Duretz and Gerya*, 2013].

Failure of an intact subducting plate typically starts at one side and propagates toward the other side of the slab over a certain time period [*Wortel and Spakman*, 2000]. During such slab tearing, the total slab pull force is focused on the remaining intact portion. This portion steadily decreases in size (due to the advancing tearing), which supports the lateral continuation of plate failure.

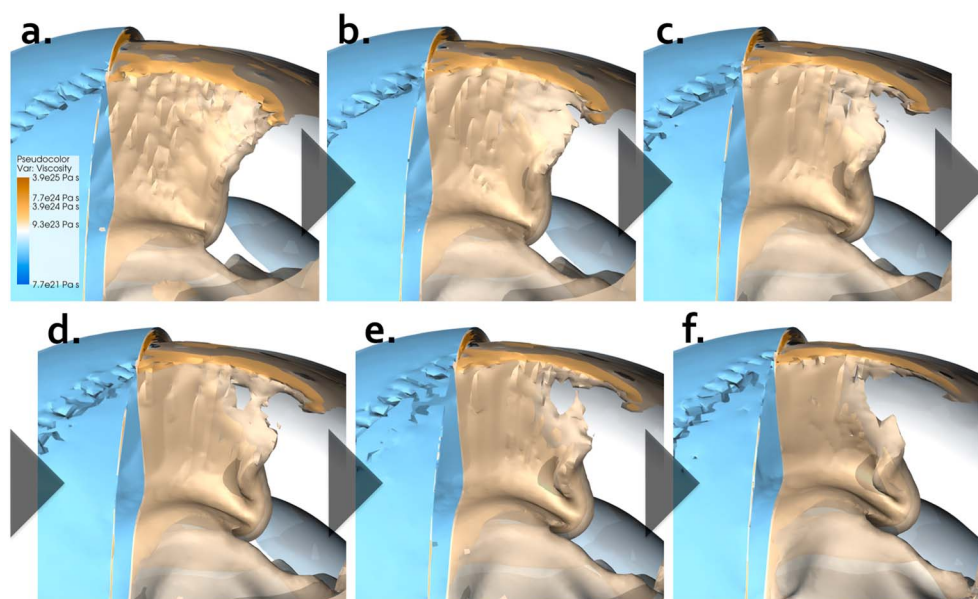


Figure 9. (a–f) Evolution of slab tearing shown in a global spherical 3-D model by contours of viscosity. The stiff downgoing plate (yellow) is moving toward the observer before subduction and is starting to laterally tear apart at depth while the remaining intact part is still subducting.

Slab break off by lateral tear propagation does occur in the models presented in this study (Figure 9). The cause of such subduction shutoff here cannot, however, be a collision including a continent (as mentioned earlier) because of the absence of a continent. Slab tearing might thus be due to (a) a reorientation of plate motion; (b) the approach of young, less negatively buoyant lithosphere; or (c) an increase in subduction resistance due to rearrangement of mantle flow.

The slab shown in Figure 9 starts to thin out at the lateral edge at shallow depth, which is followed by a viscous tearing from the side to its interior. Small portions inside the intact slab thereby sometimes already start to tear shortly before the main lateral tear reaches this location, thereby creating what appear to be small holes inside the slab (Figure 9d). The lateral portion of the slab that has detached vertically starts to sink faster than the connected portion and thereby folds due to accumulation of subducted material at its bottom.

4.2.1. Comparison to Observations

The slab tearing shown in Figure 9 starts at (or close to) the slab edge. Fully dynamic regional models suggest that this might be due to an asymmetric slowing down of the subducting plate [*van Hunen and Allen, 2011*]. In their case, the slowing is produced by a continental collision, whereas in the models presented here this is not possible due to the absence of continental lithosphere. Instead, downward motion of a subducting plate can slow down either by a rearrangement of global plate motions or by a decrease in the plate's age at the trench.

Slab tearing initiating from a slab edge was previously proposed to explain the geodynamic evolution of the Mediterranean-Carpathian region during the last 20–30 Ma [*Wortel and Spakman, 2000*].

Other natural examples of slab tearing involve the influence of a spreading ridge. Along the Baja California Sur plate boundary, plate motion change accommodated by a change in spreading direction may have led to slab break off [*Michaud et al., 2006*]. In the Patagonian part of the Andean collision zone [*Guivel et al., 2006*] the ridge segment approached the subduction trench after a period of ongoing plate convergence that increased the tectonic coupling between the subducting and overriding plates. This led to deformation of the upper plate and to resistance against further sinking of the downgoing plate. After the ridge collision with the trench, the slab started to break off further down in the subduction zone leaving a young segment at the surface that was previously part of the subducting plate. The slab tearing is thereby related to emplacement of alkali basalt and ridge subduction-related lavas near the trench at the surface (e.g., Taitao Peninsula).

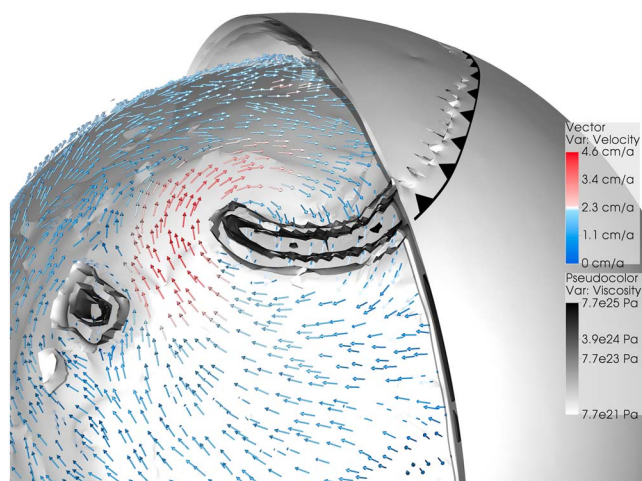


Figure 10. Subduction-induced toroidal mantle flow around the slab edge indicated by small blue (slow velocity) and red (fast velocity) arrows. Shown are viscosity isosurfaces (grey color map) and indications for the subduction trench location.

4.3. Subduction-Induced Mantle Flow

Two main modes of mantle flow driven by subduction can be observed in the experiments presented here. The first is the two-dimensional poloidal flow that is induced by the vertical sinking of the slab. This occurs on both sides of the slab, atop in the mantle wedge and behind it, therefore driving both the subducting and the overriding plate toward the trench. This flow can also be observed in 2-D models of mantle convection [see *Cramer*, 2013, Chapter 3]. The second is toroidal flow, which only occurs in three-dimensional convection with laterally variable viscosity. This operates in a horizontal direction and is often termed mantle return flow. The

inclined sinking of a slab (a characteristic of single-sided subduction) in combination with trench retreat creates an overpressure in the mantle underneath and a negative pressure above it, which causes mantle material to escape from behind the slab to its other side (see also Figure 6). An efficient way for the mantle to do that is to flow around the lateral slab edges. As a result, there is trench-parallel flow behind the slab and a strong toroidal flow at the edges (Figures 8 and 10). This subduction-induced mantle flow can retroactively deform the slab causing an arcuate geometry that is also visible at the trench at the surface.

4.4. “Back-Slab Spiral Flow”

The combination of the trench-parallel flow (due to slab retreat) and poloidal flow (due to slab sinking) causes a trench-parallel spiral flow in the back of the sinking slab (Figure 11). This feature is characterized by downward motion close to the sinking portion of the plate ($x < 2 \times d_{x,\text{slab}}$) and upward motion farther away ($x > 2 \times d_{x,\text{slab}}$) in a vertical cross section, where x is the distance away from the slab and $d_{x,\text{slab}}$ is the slab thickness. In a horizontal section, a purely trench-parallel flow is prevented by a directional component toward the slab at shallow depths ($z < 0.5 \times d_{z,\text{slab}}$) and away from the slab in deeper regions of the mantle ($z > 0.5 \times d_{z,\text{slab}}$), where z is the depth and $d_{z,\text{slab}}$ is the vertical slab extent. The flow spiral is typically located behind central portions of the slab and laterally limited by the onset of toroidal flow motions around the slab edges.

4.4.1. Link to Observations

The spiral-shaped flow in the mantle behind a subduction zone (Figure 12) arises due to the combination of downward flow close to the slab (due to viscous coupling with the sinking slab), upward flow farther from the slab (return flow) and horizontal, trench-parallel flow (due to slab retreat). This back-slab spiral flow exists laterally as far as the slab extends. A common conception is that horizontal flow in the back-slab region is purely trench parallel. This observed spiral flow, however, adds a small component toward the trench/slab at shallow depth and away from the trench/slab at larger depth, something that could potentially be observed in measurements of seismic anisotropy.

The spatial extend of this spiral flow is strongly dependent on the amount of viscous coupling between the sinking slab and the subjacent mantle. The actual amount of viscous coupling is, however, still under debate [see, e.g., *Long*, 2013]. The models presented here are entirely Newtonian. Dislocation creep is, however, likely to be activated for flow around vertically sinking slabs in the upper mantle. Such non-Newtonian deformation might reduce the viscous slab-mantle coupling and hence the size of the flow spiral.

4.5. Slab Tunneling

For wider slabs, however, flow around both edges is insufficient to allow all subslab mantle to escape; material far from a slab edge accumulates in an evolving notch in the middle of the slab (i.e., in a “stagnant zone”). In the case of a further retreating, intact slab, this portion of the mantle has no choice other than to deform

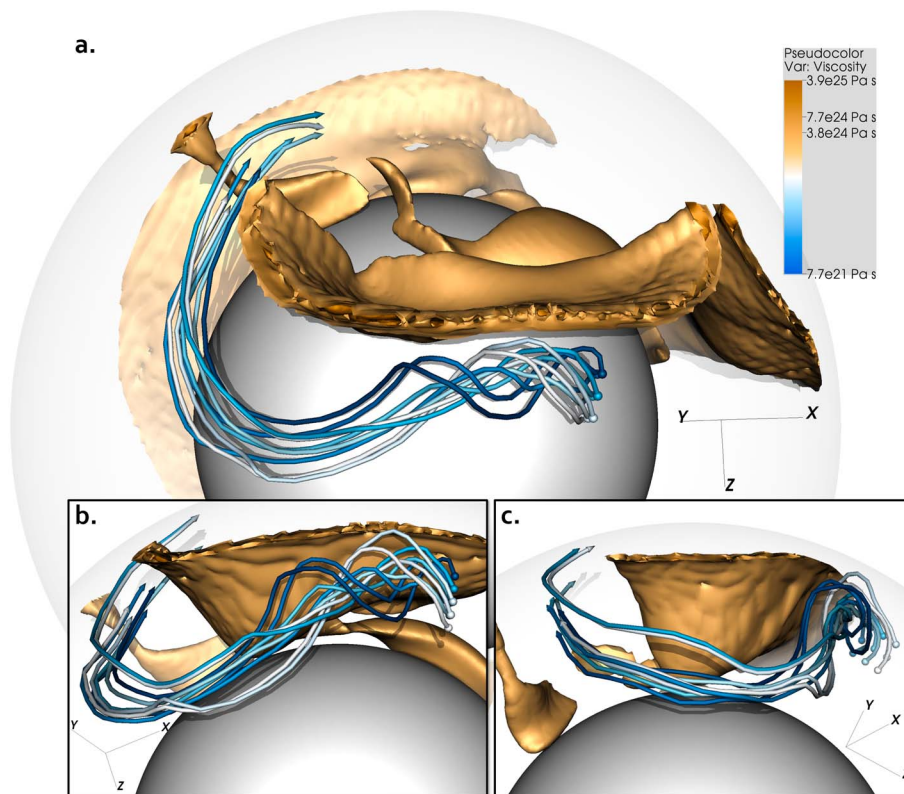


Figure 11. Spiral mantle flow in the back-slab region shown in a global spherical 3-D model in (a) global top view, (b) horizontal view toward the back of the slab, and (c) side view. Viscosity isosurfaces show slabs (brown) sinking toward the CMB (core mantle boundary; grey), whereby the surface plates are visually cut away. Color map values are nondimensional. Retreating slabs cause a spiral mantle flow at their backside, which ends up in a toroidal flow around the slab edges. Separate bluish-colored tubes indicate instantaneous flow lines starting from several differently located seeding points (bluish-colored spheres).

the central portion of the sinking slab. At first this portion of the slab is forced to sink at a lower angle. If this is not sufficient to allow for a progressive slab rollback, the slab is deformed toward a tunnel-like structure (Figure 13). This “slab tunnel” then allows the mantle material to escape to the other side of the slab, which in turn enables further slab rollback. Similar to the toroidal return-flow, the tunnel creates a bottleneck that requires high-flow velocities.

The characteristics of such slab tunneling are (a) a locally flat slab and (b) a strong slab-perpendicular flow right underneath the kink between two arcs of a double-arcuate (or more) subduction trench.

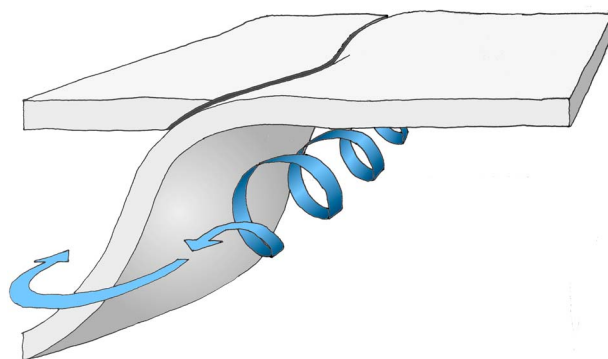


Figure 12. Three-dimensional sketch of the back-slab flow spiral.

4.5.1. Link to Observations

The depth of the slab tunnel is around 1200 km. In the Earth, the upper mantle transition zone (410–660 km depth) would certainly strongly influence its development. Nature-like plates, however, are thinner than in the model presented here (see section 6 for details). Thinner plates are bending more readily, and a feature like slab tunneling that is strongly controlled by bending would decrease in spatial extent.

The occurrence of this slab tunneling on Earth is supported by the occurrence

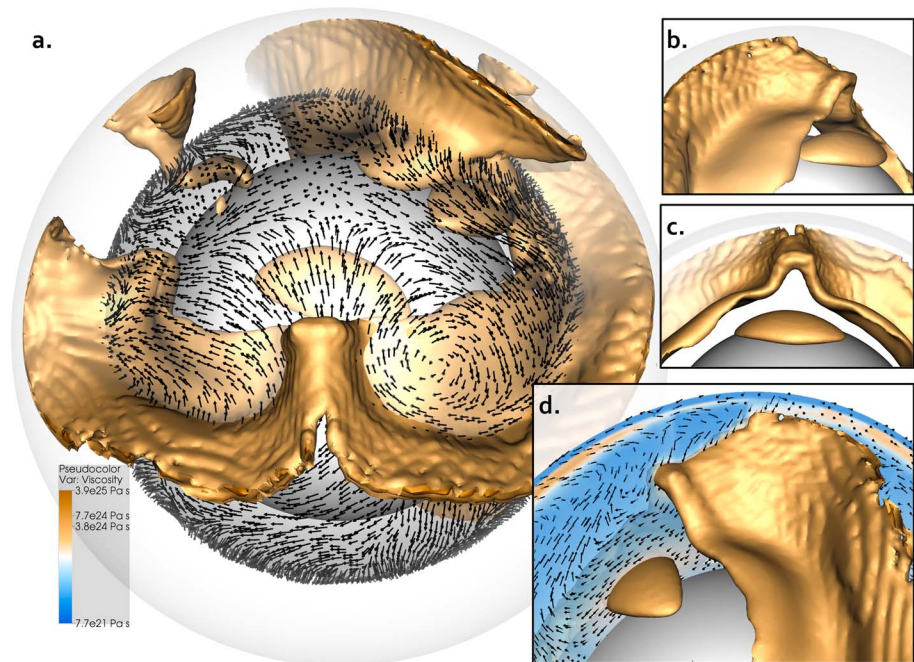


Figure 13. Slab tunneling shown in a global spherical 3-D model in (a) global top view including a horizontal slice indicating mantle flow (black arrows) through the tunnel, (b) right-hand side view, (c) front view, and (d) left-hand side view including a vertical slice through the tunnel structure including arrows indicating viscosity and mantle flow direction (black arrows). Viscosity isosurfaces show slabs (brown) sinking toward the CMB (core mantle boundary; transparent grey) that are characteristically deformed due to induced upper mantle flow (black arrows). Wide slabs inhibit toroidal edge flow of mantle material and form slab tunnels in order to displace mantle material from below the slab to the other side, thereby creating locally flat subduction and a hinge in the trench above.

of regional trench advance (or a reduced trench retreat compared to adjacent arc segments) in the interior of wide slabs [Stegman *et al.*, 2010a, 2010b]. A possible slab tunneling is further supported by observations of flat subduction in places of wide subduction zones like the South America subduction zone [Gutscher *et al.*, 2000].

The observed mantle seismic anisotropy directions in the mantle wedge and in slab regions on present-day Earth are shown in Figure 1 [Long and Becker, 2010]. Inferred trench-perpendicular flow in the subduction hinge in the middle of the South America subduction zone and trench-parallel flow at both sides support a possible occurrence of slab tunneling there. Observations of seismicity in the downgoing plate portions provide some indication on the slab dip along strike [e.g., Martinod *et al.*, 2010]: At shallow depth (<200 km), the slab is steeper at the Bolivian kink than it is in the north (i.e., Peru) or in the south (i.e., central Chile), which would contradict the occurrence of slab tunneling. At greater depth (>200 km), however, there is weak indication that the situation is the other way round, where the slab at the Bolivian kink might sink at a lower angle compared to its surroundings.

Another wide subduction zone characterized by a multiarcuate shape that would allow for slab tunneling is the Aleutians and Kamchatka subduction zone. The Aleutian-Kamchatka juncture is, however, believed to be undergoing slab tearing or at least a significant slab thinning [Davaille and Lees, 2004] in the region where a slab tunnel would form. Observations show a lack of deep seismicity (i.e., 200–600 km) at the slab kink [Gorbatov *et al.*, 1997].

4.6. Model Geometry

Results obtained by models in two fundamentally different 3-D geometries, Cartesian and spherical shell, are presented here. Many aspects of system behavior are similar in the two geometries, and thus, both yield important insights into the temporal evolution of spreading ridges, slab propagation and deformation, and subduction-related mantle flow. Spherical geometry is more natural, and an important feature of it is the decreasing surface area with increasing depth, which imposes geometrical restrictions on sinking slabs. This seems to make single-sided subduction occur more naturally: a long, linear, vertically sinking slab is

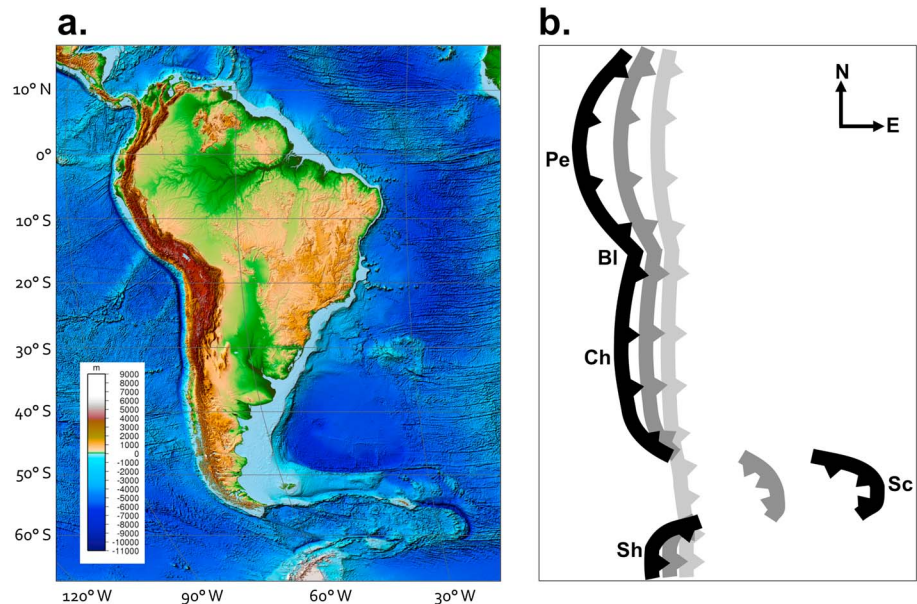


Figure 14. (a) Topography of South America and surrounding seafloor showing the range from low elevated trenches (dark blue) to high elevated orogens (dark brown). (Source: NOAA, <http://www.ngdc.noaa.gov/mgg/global/global.html>). (b) Sketch of the subduction trench evolution for a conceptual model of the dynamic evolution of the Peru (Pe), Bolivian (Bl), Chile (Ch), Scotia (Sc), and South Shetland (Sh) subduction zones that is in agreement with observations compiled in *Barker [2001]*.

disfavored due to the along-strike compression that would be needed. Similarly, spherical geometry seems to favor arcuate subduction even more than Cartesian geometry. Additionally, of course, using a full spherical shell also avoids a somewhat arbitrary choice of aspect ratio in a Cartesian box.

5. Implications for Present-Day Earth

The 4-D experiments presented here can help our understanding of subduction dynamics to progress beyond the common view of a purely 2-D subduction system. Below, we apply insights gained from our numerical experiments to two subduction systems on present-day Earth and suggest a conceptual model for both the evolution of the South America subduction zone and the onset of the South Sandwich subduction zone.

5.1. South America Subduction Zone Evolution

As mentioned earlier, the South America subduction zone is a prominent feature on present-day Earth that shows clear signs of trench migration and deformation through its double-arcuate shape. The deep Chilean trench in the west is adjacent to the steep slope and wide elevated plateau of the Central Andes that is finally flanked by a gentle slope subsiding gradually toward the Brazilian Shield in the East. The topography of the Andean orogen is most prominent in its central part, exactly at the kink between the two arcuate trenches (Figure 14a). The last mountain building phase began 26 Ma ago [see, e.g., *Gregory-Wodzicki, 2000*, and references therein] due to crustal thickening induced by tectonic shortening [*Isacks, 1988; Lamb and Hoke, 1997*]. Several models have been proposed to explain this kinematic evolution of the Central Andes by geologic records [e.g., *Lamb and Hoke, 1997*], seismic observations [e.g., *Yuan et al., 2000*], and modeling [e.g., *Isacks, 1988; Wdowinski and Bock, 1994*].

The high retreat rate in the center of both trench arcs that are outlined in Figure 14b (i.e., Peru and Chile in the north and south of the Bolivian kink) contrasts to that in the central Bolivian part, where the trench is retreating at a lower rate [*Schellart et al., 2008*]. This is the region above the previously called “stagnation point” [*Russo and Silver, 1994*], where mantle material cannot escape around the slab edges due to its large width and is instead accumulated (see section 4.5.1). The dynamics can therefore be best understood if the Bolivian kink is thought to be the reference frame for trench motion; that is, it does not move. The trench portions in the north and south do, however, retreat at a certain speed. The continental lithosphere (which is generally believed to be weaker than oceanic lithosphere) is thereby dragged eastward by trench suction.

The central part of the continent is, however, stopped by the static Bolivian trench portion that can be considered to be a backstop for eastward motion. As the continent (as a whole) moves eastward, it has to deform strongly in its central part, which might result in a highly elevated plateau like the Central Andes.

5.2. South Sandwich Subduction Zone Onset

Another intriguing feature in our dynamical models, which may provide some understanding about the evolution of subduction settings on Earth, is subduction-polarity reversal as shown in Figure 5. There, a section of the initially intact subduction zone undergoes a switch in subduction polarity, leading to a subsequent separation and an autonomous small subduction zone. The subduction of a spreading ridge was the trigger for this particular event. On Earth, this might have happened to an initially intact South America-South Shetland subduction system as outlined in the sketch of Figure 14b. We suggest that around 40 Ma ago, the continental connection between South America and the Antarctic Peninsula (light grey trench) was separated by a subduction-polarity reversal and subsequent lateral detachment of the South Sandwich subduction zone (grey trench) that evolved into the present-day geometry (black trench). This model is in good agreement with previous regional plate reconstructions derived from a large suite of data (regional geology and geophysics, earthquake seismology, satellite altimetry, global plate analyses) that are compiled in *Barker* [2001]. Analogous to the model evolution in Figure 5, the collision of the subduction trench with the Chile ridge is believed to have played the role of the trigger for the onset of the subduction-polarity reversal there [*Barker*, 2001].

6. Model Strengths and Limitations

The goal of this study is to explore the dynamical evolution of Earth-like subduction zones in a global context using a modeling approach that is as simplified as possible while still retaining key first-order physical characteristics, which we consider to be a strongly temperature dependent, viscoplastic rheology, and a free surface. Hence, the model presented here is not intended to be an exact replica of an Earth-like rocky planet, and the simplifications may cause some disagreements with nature. We, therefore, evaluate model features below.

Compared to previous 3-D spherical models that include self-consistent plate tectonics [e.g., *van Heck and Tackley*, 2008; *Foley and Becker*, 2009; *Nakagawa et al.*, 2010; *Rolf and Tackley*, 2011], features that are improved and brought to good agreement with available observations are (i) the single-sided geometry of subduction zones, which is enabled by a free surface; (ii) the arcuate slab/trench geometry; (iii) the nearly trench-parallel back-slab flow in central parts of the subduction zone; and (iv) the toroidal mantle flow around slab edges. The latter three features are facilitated by single-sided subduction.

In contrast, model features that are not in good agreement with natural observations are (i) the plate thickness, which is larger than realistic due to a low effective Rayleigh number; (ii) transform faults, which are too wide due to not including strain weakening or strain rate weakening in the model; and (iii) the low strength of the lithosphere compared to laboratory constraints [*Kohlstedt et al.*, 1995], which is needed to prevent a stagnant lid regime. The latter discrepancy is common to all dynamically self-consistent mantle convection models and regional subduction models that do not have preinserted weak zones and might be due to the influence of water, which, for example, causes thermal cracking and hydration [*Korenaga*, 2007]. This argument might, however, not be applicable to the central parts of wide plates (e.g., the central Pacific plate), since *Zhong and Watts* [2013] inferred from a comparison between models and observations of lithospheric flexure and seismicity (caused by the Hawaiian Islands loading) that the friction coefficient inside the oceanic lithosphere is $\mu > 0.25$.

Other simplifying assumptions made here, which may cause some other disagreements between model and nature, are (i) the incompressibility of the mantle under the Boussinesq approximation, with constant physical properties except for viscosity; (ii) a simplified viscoplastic rheology, with no elasticity (which may be important in the lithosphere) or dislocation creep; (iii) assuming a compositionally homogeneous lithosphere (i.e., no continents); (iv) the absence of basal heating and internal heating that is constant in space and time; (v) the relatively low effective Rayleigh number; and (vi) the absence of phase transitions (e.g., in the transition zone).

7. Conclusions

The models presented here aim at a better understanding of the spontaneous migration of subduction trenches and spreading ridges and the corresponding mantle flow at depth. Therefore, 3-D global models of mantle convection that allow for self-consistent dynamics through long time periods are explored. Two model geometries are presented: 3-D Cartesian and 3-D spherical shell.

Experiments conducted in a Cartesian domain display several interesting behaviors, particularly (i) the spontaneous development of arcuate trench curvature, (ii) a partial polarity reversal along a connected subduction zone, (iii) the spontaneous development of spreading ridge offsets with (iv) transform features characterizing such offsets, and (v) subduction-related mantle flow containing a large component of toroidal motion.

Experiments in a 3-D spherical shell additionally (i) display a greater tendency for arcuate subduction, (ii) evolve trench geometries varying between single-arc and multiple-arc shapes, (iii) display subduction-polarity reversals, (iii) display subduction-induced, three-dimensional mantle flow that includes back-slab spiral flow, and (iv) newly discovered slab tunneling.

We present conceptual models—from a geodynamics point of view—for both the evolution of the South America subduction zone that is strongly linked to subduction-induced mantle flow and the onset of the South Sandwich subduction zone caused by a subduction-polarity reversal.

In conclusion, both Cartesian and spherical models self-consistently develop subduction-related features that can directly be linked to observations in nature and thus lead to a better understanding of the causes of present-day structures observed on Earth.

Acknowledgments

This work was supported by SNF grant 20TO21-120535 as part of the TOPO-EUROPE program. This work was supported by a grant from the Swiss National Supercomputing Centre (CSCS) under project ID s272. Some calculations were performed on ETHs Brutus high-performance computing cluster. The authors thank the Editors, Paul Tregoning and Shijie Zhong, and an anonymous reviewer for their constructive comments.

References

- Barker, P. F. (2001), Scotia Sea regional tectonic evolution: Implications for mantle flow and palaeocirculation, *Earth Sci. Rev.*, *55*(1-2), 1–39.
- Becker, T. W., C. Faccenna, R. J. O'Connell, and D. Giardini (1999), The development of slabs in the upper mantle: Insights from numerical and laboratory experiments, *J. Geophys. Res.*, *104*(B7), 15,207–15,226.
- Bellahsen, N., C. Faccenna, and F. Funiciello (2005), Dynamics of subduction and plate motion in laboratory experiments: Insights into the "plate tectonics" behavior of the Earth, *J. Geophys. Res.*, *110*, B01401, doi:10.1029/2004JB002999.
- Bercovici, D. (1995), A source-sink model of the generation of plate tectonics from non-Newtonian mantle flow, *J. Geophys. Res.*, *100*(B2), 2013–2030.
- Bercovici, D., and Y. Ricard (2005), Tectonic plate generation and two-phase damage: Void growth versus grain size reduction, *J. Geophys. Res.*, *110*, B03401, doi:10.1029/2004JB003181.
- Bird, P. (2003), An updated digital model of plate boundaries, *Geochem. Geophys. Geosyst.*, *4*(3), 1027, doi:10.1029/2001GC000252.
- Burkett, E. R., and M. I. Billen (2009), Dynamics and implications of slab detachment due to ridge-trench collision, *J. Geophys. Res.*, *114*, B12402, doi:10.1029/2009JB006402.
- Burkett, E. R., and M. I. Billen (2010), Three-dimensionality of slab detachment due to ridge-trench collision: Laterally simultaneous boudinage versus tear propagation, *Geochem. Geophys. Geosyst.*, *11*, Q11012, doi:10.1029/2010GC003286.
- Capitania, F., G. Morra, and S. Goes (2007), Dynamic models of downgoing plate-buoyancy driven subduction: Subduction motions and energy dissipation, *Earth Planet. Sci. Lett.*, *262*(1-2), 284–297.
- Capitania, F. A., G. Morra, and S. Goes (2009), Dynamics of plate bending at the trench and slab-plate coupling, *Geochem. Geophys. Geosyst.*, *10*, Q04002, doi:10.1029/2008GC002348.
- Chemenda, A. I., J.-P. Burg, and M. Mattauer (2000), Evolutionary model of the Himalaya-Tibet system: Geopoem: Based on new modelling, geological and geophysical data, *Earth Planet. Sci. Lett.*, *174*(3-4), 397–409.
- Childs, H., E. S. Brugger, K. S. Bonnell, J. S. Meredith, M. Miller, B. J. Whitlock, and N. Max (2005), A contract-based system for large data visualization, *Proceedings of IEEE Visualization 2005*, pp. 190–198, Minneapolis, Minnesota.
- Christensen, U. R. (1996), The influence of trench migration on slab penetration into the lower mantle, *Earth Planet. Sci. Lett.*, *140*(1-4), 27–39.
- Conrad, C. P., and C. Lithgow-Bertelloni (2002), How mantle slabs drive plate tectonics, *Science*, *298*(5591), 207–209, doi:10.1126/science.1074161.
- Cramer, F. (2013), The interaction between subduction-related mantle currents and surface topography, PhD thesis, ETH Zurich.
- Cramer, F., P. J. Tackley, I. Meilick, T. V. Gerya, and B. J. P. Kaus (2012a), A free plate surface and weak oceanic crust produce single-sided subduction on Earth, *Geophys. Res. Lett.*, *39*, L03306, doi:10.1029/2011GL050046.
- Cramer, F., H. Schmeling, G. J. Golabek, T. Duret, R. Orendt, S. J. H. Buitter, D. A. May, B. J. P. Kaus, T. V. Gerya, and P. J. Tackley (2012b), A comparison of numerical surface topography calculations in geodynamic modelling: An evaluation of the "sticky air" method, *Geophys. J. Int.*, *189*(1), 38–54, doi:10.1111/j.1365-246X.2012.05388.x.
- Davaille, A., and J. M. Lees (2004), Thermal modeling of subducted plates: Tear and hotspot at the Kamchatka corner, *Earth Planet. Sci. Lett.*, *226*(3-4), 293–304.
- Davies, G. F. (1995), Penetration of plates and plumes through the mantle transition zone, *Earth Planet. Sci. Lett.*, *133*(3-4), 507–516.
- Davies, J. H., and D. J. Stevenson (1992), Physical model of source region of subduction zone volcanics, *J. Geophys. Res.*, *97*(B2), 2037–2070.
- DeMets, C., R. G. Gordon, and D. F. Argus (2010), Geologically current plate motions, *Geophys. J. Int.*, *181*(1), 1–80.
- Duret, T., and T. Gerya (2013), Slab detachment during continental collision: Influence of crustal rheology and interaction with lithospheric delamination, *Tectonophysics*, *602*, 124–140, doi:10.1016/j.tecto.2012.12.024.

- Duret, T., S. M. Schmalholz, and T. V. Gerya (2012), Dynamics of slab detachment, *Geochem. Geophys. Geosyst.*, *13*, Q03020, doi:10.1029/2011GC004024.
- Elsasser, W. M. (1971), Sea-floor spreading as thermal convection, *J. Geophys. Res.*, *76*(5), 1101–1112.
- Enns, A., T. W. Becker, and H. Schmeling (2005), The dynamics of subduction and trench migration for viscosity stratification, *Geophys. J. Int.*, *160*(2), 761–775.
- Foley, B. J., and T. W. Becker (2009), Generation of plate-like behavior and mantle heterogeneity from a spherical, viscoplastic convection model, *Geochem. Geophys. Geosyst.*, *10*, Q08001, doi:10.1029/2009GC002378.
- Forsyth, D., and S. Uyeda (1975), On the relative importance of the driving forces of plate motion*, *Geophys. J. R. Astron. Soc.*, *43*(1), 163–200.
- Fukao, Y., and M. Obayashi (2013), Subducted slabs stagnant above, penetrating through, and trapped below the 660 km discontinuity, *J. Geophys. Res. Solid Earth*, *118*, 5920–5938, doi:10.1002/2013JB010466.
- Funiciello, F., C. Faccenna, D. Giardini, and K. Regenauer-Lieb (2003), Dynamics of retreating slabs: 2. Insights from three-dimensional laboratory experiments, *J. Geophys. Res.*, *108*(B4), 2207, doi:10.1029/2001JB000896.
- Funiciello, F., C. Faccenna, and D. Giardini (2004), Role of lateral mantle flow in the evolution of subduction systems: Insights from laboratory experiments, *Geophys. J. Int.*, *157*(3), 1393–1406.
- Funiciello, F., C. Faccenna, A. Heuret, S. Lallemand, E. Di Giuseppe, and T. Becker (2008), Trench migration, net rotation and slab-mantle coupling, *Earth Planet. Sci. Lett.*, *271*(1–4), 233–240.
- Garfunkel, Z., C. A. Anderson, and G. Schubert (1986), Mantle circulation and the lateral migration of subducted slabs, *J. Geophys. Res.*, *91*(B7), 7205–7223.
- Gerya, T. (2012), Origin and models of oceanic transform faults, *Tectonophysics*, *522–523*, 34–54.
- Gerya, T. V., J. A. Connolly, and D. A. Yuen (2008), Why is terrestrial subduction one-sided?, *Geology*, *36*(1), 43–46, doi:10.1130/G24060A.1.
- Gorbatov, A., V. Kostoglodov, G. Suárez, and E. Gordeev (1997), Seismicity and structure of the Kamchatka subduction zone, *J. Geophys. Res.*, *102*(B8), 17,883–17,898.
- Gregory-Wodzicki, K. M. (2000), Uplift history of the Central and Northern Andes: A review, *Geol. Soc. Am. Bull.*, *112*(7), 1091–1105.
- Guivel, C., et al. (2006), Miocene to Late Quaternary Patagonian basalts (46–47°S): Geochronometric and geochemical evidence for slab tearing due to active spreading ridge subduction, *J. Volcanol. Geotherm. Res.*, *149*(3–4), 346–370.
- Gurnis, M., and B. H. Hager (1988), Controls of the structure of subducted slabs, *Nature*, *335*, 317–321, doi:10.1038/335317a0.
- Gutscher, M.-A., W. Spakman, H. Bijwaard, and E. R. Engdahl (2000), Geodynamics of flat subduction: Seismicity and tomographic constraints from the Andean margin, *Tectonics*, *19*(5), 814–833.
- Houseman, G. A., and D. Gubbins (1997), Deformation of subducted oceanic lithosphere, *Geophys. J. Int.*, *131*(3), 535–551.
- Isacks, B. L. (1988), Uplift of the Central Andean Plateau and bending of the Bolivian Orocline, *J. Geophys. Res.*, *93*(B4), 3211–3231.
- Kaula, W. M. (1975), Absolute plate motions by boundary velocity minimizations, *J. Geophys. Res.*, *80*(2), 244–248.
- Kincaid, C., and P. Olson (1987), An experimental study of subduction and slab migration, *J. Geophys. Res.*, *92*(B13), 13,832–13,840.
- Kohlstedt, D. L., B. Evans, and S. J. Mackwell (1995), Strength of the lithosphere: Constraints imposed by laboratory experiments, *J. Geophys. Res.*, *100*(B9), 17,587–17,602.
- Korenaga, J. (2007), Thermal cracking and the deep hydration of oceanic lithosphere: A key to the generation of plate tectonics?, *J. Geophys. Res.*, *112*, B05408, doi:10.1029/2006JB004502.
- Lamb, S., and L. Hoke (1997), Origin of the high plateau in the Central Andes, Bolivia, South America, *Tectonics*, *16*(4), 623–649.
- Long, M. D. (2013), Constraints on subduction geodynamics from seismic anisotropy, *Rev. Geophys.*, *51*, 76–112, doi:10.1002/rog.20008.
- Long, M. D., and T. W. Becker (2010), Mantle dynamics and seismic anisotropy, *Earth Planet. Sci. Lett.*, *297*(3–4), 341–354.
- Long, M. D., and P. G. Silver (2009), Mantle flow in subduction systems: The subslab flow field and implications for mantle dynamics, *J. Geophys. Res.*, *114*, B10312, doi:10.1029/2008JB006200.
- Long, M. D., and E. A. Wirth (2013), Mantle flow in subduction systems: The mantle wedge flow field and implications for wedge processes, *J. Geophys. Res. Solid Earth*, *118*, 583–606, doi:10.1002/jgrb.50063.
- Martinod, J., L. Husson, P. Roperch, B. Guillaume, and N. Espurt (2010), Horizontal subduction zones, convergence velocity and the building of the Andes, *Earth Planet. Sci. Lett.*, *299*(3–4), 299–309.
- Matsumoto, T., and Y. Tomoda (1983), Numerical simulation of the initiation of subduction at the fracture zone, *J. Phys. Earth*, *31*(3), 183–194.
- Michaud, F., et al. (2006), Oceanic-ridge subduction vs. slab break off: Plate tectonic evolution along the Baja California Sur continental margin since 15 Ma, *Geology*, *34*(1), 13–16.
- Morra, G., K. Regenauer-Lieb, and D. Giardini (2006), Curvature of oceanic arcs, *Geology*, *34*(10), 877–880.
- Nakagawa, T., P. J. Tackley, F. Deschamps, and J. A. Connolly (2010), The influence of MORB and harzburgite composition on thermo-chemical mantle convection in a 3-D spherical shell with self-consistently calculated mineral physics, *Earth Planet. Sci. Lett.*, *296*(3–4), 403–412.
- Nemcok, M., L. Pospisil, J. Lexa, and R. Donelick (1998), Tertiary subduction and slab break-off model of the Carpathian-Pannonian regions, *Tectonophysics*, *295*(3–4), 307–340.
- Paczkowski, K. (2012), Dynamic analysis of modifications to simple plate tectonics theory, PhD thesis, Yale University.
- Regard, V., C. Faccenna, J. Martinod, and O. Bellier (2005), Slab pull and indentation tectonics: Insights from 3D laboratory experiments, *Phys. Earth Planet. Inter.*, *149*(1–2), 99–113.
- Rolf, T., and P. J. Tackley (2011), Focussing of stress by continents in 3D spherical mantle convection with self-consistent plate tectonics, *Geophys. Res. Lett.*, *38*, L18301, doi:10.1029/2011GL048677.
- Russo, R. M., and P. G. Silver (1994), Trench-parallel flow beneath the Nazca plate from seismic anisotropy, *Science*, *263*(5150), 1105–1111.
- Schellart, W., and N. Rawlinson (2010), Convergent plate margin dynamics: New perspectives from structural geology, geophysics and geodynamic modelling, *Tectonophysics*, *483*(1–2), 4–19.
- Schellart, W., D. Stegman, and J. Freeman (2008), Global trench migration velocities and slab migration induced upper mantle volume fluxes: Constraints to find an Earth reference frame based on minimizing viscous dissipation, *Earth Sci. Rev.*, *88*(1–2), 118–144.
- Schellart, W. P. (2004), Kinematics of subduction and subduction-induced flow in the upper mantle, *J. Geophys. Res.*, *109*, B07401, doi:10.1029/2004JB002970.
- Schmeling, H., et al. (2008), A benchmark comparison of spontaneous subduction models—Towards a free surface, *Phys. Earth Planet. Inter.*, *171*(1–4), 198–223, doi:10.1016/j.pepi.2008.06.028.
- Stampfli, G., and G. Borel (2002), A plate tectonic model for the Paleozoic and Mesozoic constrained by dynamic plate boundaries and restored synthetic oceanic isochrons, *Earth Planet. Sci. Lett.*, *196*(1–2), 17–33.

- Stegman, D., R. Farrington, F. Capitanio, and W. Schellart (2010a), A regime diagram for subduction styles from 3-D numerical models of free subduction, *Tectonophysics*, *483*(1-2), 29–45.
- Stegman, D., W. Schellart, and J. Freeman (2010b), Competing influences of plate width and far-field boundary conditions on trench migration and morphology of subducted slabs in the upper mantle, *Tectonophysics*, *483*(1-2), 46–57.
- Stegman, D. R., J. Freeman, W. P. Schellart, L. Moresi, and D. May (2006), Influence of trench width on subduction hinge retreat rates in 3-D models of slab rollback, *Geochem. Geophys. Geosyst.*, *7*, Q03012, doi:10.1029/2005GC001056.
- Tackley, P. J. (1998), Self-consistent generation of tectonic plates in three-dimensional mantle convection, *Earth Planet. Sci. Lett.*, *157*(1-2), 9–22.
- Tackley, P. J. (2000), Self-consistent generation of tectonic plates in time-dependent, three-dimensional mantle convection simulations—Part 1: Pseudo-plastic yielding, *Geochem. Geophys. Geosyst.*, *1*(8), 1–45, doi:10.1029/2000GC000036.
- Tackley, P. J. (2008), Modelling compressible mantle convection with large viscosity contrasts in a three-dimensional spherical shell using the yin-yang grid, *Phys. Earth Planet. Inter.*, *171*(1-4), 7–18, doi:10.1016/j.pepi.2008.08.005.
- van Heck, H. J., and P. J. Tackley (2008), Planforms of self-consistently generated plates in 3D spherical geometry, *Geophys. Res. Lett.*, *35*, L19312, doi:10.1029/2008GL035190.
- van Hunen, J., and M. B. Allen (2011), Continental collision and slab break-off: A comparison of 3-D numerical models with observations, *Earth Planet. Sci. Lett.*, *302*(1-2), 27–37.
- van Keken, P. E. (2003), The structure and dynamics of the mantle wedge, *Earth Planet. Sci. Lett.*, *215*(3-4), 323–338.
- Wdowinski, S., and Y. Bock (1994), The evolution of deformation and topography of high elevated plateaus: 2. Application to the Central Andes, *J. Geophys. Res.*, *99*(B4), 7121–7130.
- Wortel, M. J. R., and W. Spakman (2000), Subduction and slab detachment in the Mediterranean-Carpathian region, *Science*, *290*(5498), 1910–1917, doi:10.1126/science.290.5498.1910.
- Yuan, X., et al. (2000), Subduction and collision processes in the Central Andes constrained by converted seismic phases, *Nature*, *408*, 958–961.
- Zhong, S., and M. Gurnis (1995), Mantle convection with plates and mobile, faulted plate margins, *Science*, *267*(5199), 838–843.
- Zhong, S., and A. B. Watts (2013), Lithospheric deformation induced by loading of the Hawaiian Islands and its implications for mantle rheology, *J. Geophys. Res. Solid Earth*, *118*, 6025–6048, doi:10.1002/2013JB010408.